Optimization of Observation Strategy to Improve Re-entry Prediction of Objects in HEO

M. Rasotto and G. Di Mauro
Dinamica Srl, Italy
M. Massari and P. Di Lizia
Politecnico di Milano, Department of Aerospace Science and Technology, Italy
R. Armellin
Surrey Space Centre, University of Surrey, United Kingdom
Q. Funke
IMS Space Consultancy GMBH c/o ESA-ESOC, Germany
T. Flohrer
European Space Operations Center (ESOC), Germany

ABSTRACT

During the last decade the number of space debris moving on high elliptical orbit (HEO) has grown fast. Many of these resident space objects (RSO) consist of medium and large spent upper stages of launch vehicles, whose atmosphere re-entry might violate on-ground casualty risk constraints. Increasing the accuracy of re-entry predictions for this class of RSO is therefore a key issue to limit the hazards on the Earth assets.
Traditional computational methods are mainly based on the exploitation of Two Line Elements (TLEs), provided by the United States Strategic Command (USSTRATCOM) and currently the only public data source available for these kind of analyses. TLE data however, are characterized by low accuracies, and in general come without any uncertainty information, thus limiting the achievable precision of the re-entry estimates. Better results on the other hand, can be obtained through the exploitation of observational data provided by one or more Earth sensors. Despite the benefits, this approach introduces a whole new set of complexities, mainly related with the design of proper observation campaigns. This paper presents a method based on evolutionary algorithms, for the optimization of observation strategies. The effectiveness of the proposed approach is demonstrated through dedicated examples, in which re-entry predictions, attainable with existing and ideal sensor architectures, are compared with corresponding results derived from TLE data.

1. INTRODUCTION

High elliptical orbits (HEO), and in particular geostationary transfer orbits (GTO), are orbits characterized by low perigee altitudes (170-650 km) and apogees close to the geo-stationary altitude (35,780 km). Thus a spent upper stage in a GTO generally passes through both the Low Earth Orbit (LEO) and Geostationary Earth Orbit (GEO) regions. Because these regions are both densely populated orbital regimes, a GTO object might collide with an operating spacecraft, damaging it and generating new space debris. In addition, spent upper stages are large bodies consisting of highly survivable components (such as propellant tanks). Thus, their atmosphere re-entry might violate the constraint on casualty risk, ([1] and [2]). In light of the above, the improvement of re-entry prediction of GTO spent upper stages is a key issue to manage both on-orbit collision risk and on-ground casualty risk.
Two Line Elements (TLEs), provided by the United States Strategic Command (USSTRATCOM), are currently the only public data source available for re-entry prediction of a space object. However, they are inaccurate and do not come with uncertainty information, i.e. a covariance matrix, [4]. In addition, provided B* parameters are merely fitting parameters used in the TLE generation process, which are typically inadequate to correctly describe the drag effects. Furthermore, the quality of TLE is not homogeneous and sometime low quality or even wrong TLE are distributed, [6]. Although some techniques exist for the proper TLE filtering ([7] and [8]), and several methods have been successfully applied for the computation of ballistic coefficients ([5] and [9]), their use remains very challenging for this kind of analyses.
An alternative approach foresees the exploitation of dedicated observation campaigns for the generation of high accuracy data, which in turn can be used to improve the orbit knowledge, and ultimately the re-entry prediction estimate. Despite the benefits, this approach introduces a whole new set of complexities, mainly related with the design of proper observation campaigns. In particular, considerations on the type, the number and the frequency of the

measurements become relevant and need to be evaluated. This is especially true for GTO objects, whose orbital configuration makes the object tracking a difficult task: in fact, an object in GTO tends to move at relatively high speed when it flies close to the Earth; on the other hand, its speed decreases to opportune values around the apogee, which is very far from the Earth surface. Therefore, planning and implementing an observation campaign often requires the design of an observation strategy through which maximize the impact of additional observations on the state and parameters estimation. For example, acquiring observations very close in time (or on a short arc of the trajectory) does not improve the orbit knowledge significantly, as the uncertainty set will grow quickly ([3]).
The main goal of the present work is to devise observation strategies for multiple sensors and sensor types/configurations to improve the re-entry prediction for a set of resident space objects (RSO). More specifically, the design of observation strategies is formulated as a multi-objective optimization problem and solved by means of automated evolutionary algorithms. Following this approach, a set of optimal solutions can be found (Pareto front), which simultaneously minimize the number of measurements and the uncertainty on re-entry epoch.
The present paper is organized as follows. Firstly, an overview of the observation simulator tool is given in Section 2, focusing in particular on the description of visibility constraints and sensor models. Section 3 is devoted to the definition of an existing architecture, i.e. an ad-hoc network of existing sensors, and ideal architectures, generated instead from a set of new prospective instruments. Then, large part of the manuscript is dedicated to Section 4, where the observation strategy optimization is presented in details. The effectiveness of the whole approach is demonstrated through some examples, reported in Section 5. Finally, the main conclusions and future developments are summarized in Section 6.

2. OBSERVATION SIMULATOR

The proper design of detection strategies for HEO objects, relies on the correct reproduction of the observation campaign, through which the necessary measurements are obtained. This typically requires a good characterization of the sensors as well as a precise description of the RSO motion. In particular, dealing with HEO objects entails the use of an accurate dynamical model, able to describe the effects of third-body perturbations, Earth's oblateness and capture the intricacies of the re-entry phase. For these reasons, a software tool, referred to as IRIS from now on, has been implemented in Matlab. As shown in Fig. 1, given the object initial state and parameters, a high-fidelity orbital propagator, referred to as AIDA, is firstly used to compute the object's trajectory. The propagated orbital motion is successively stored in a kernel file, generated through SPICE functions. Similarly, kernel files for all the available observatories are created as well, considering the given sensor's features (e.g. geodetic coordinates, accuracy etc.). Once kernels have been created, SPICE routines for the computation of relative geometry between current space object and observers are exploited: based on this result, an evaluation of the visibility constraints is performed, followed by the computation of visibility windows, observables and available measurements.

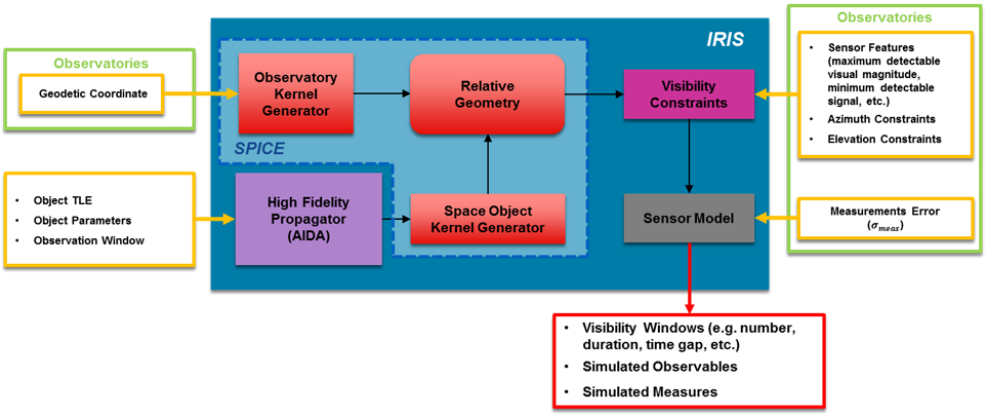

Fig. 1. IRIS tool scheme.

2.1 Visibility Constraints

The visibility constraints included in IRIS for space object detection can be categorized in two main classes:

1) *Geometrical constraints*, mainly caused by the relative position between the observatory on the Earth surface and the space object. Typical constraints belonging to this class are those associated with the admissible azimuth and elevation ranges.
2) *Observatory type constraints*, mainly due to the type and features of the selected observatories. In particular, for optical instruments:
    a) the object must be illuminated by the Sun;
    b) its brightness must exceed that of the background sky by a certain margin;
    c) the separation angle between object and Moon must be higher than a minimum value;
    d) Sun elevation must be lower than a reference value, i.e. the observation must occur during the night;
    e) the object velocity must be lower than a reference value.

    For radar, instead, the received power has to be higher than the minimum detectable signal (MDS), i.e.

$$MDS = \frac{P_t * G_{TX} * G_{RX} * \lambda^2 * \overline{RCS} * L_{TX} * L_{RX}}{(4\pi)^3 (\overline{r_{RAD}})^4} \tag{1}$$

where P_t is the transmitter power, G_{RX}/G_{RX} is the receiver/transmitter gain, L_{RX}/L_{TX} is the loss due to atmosphere disturbance in receiver/transmitter track, λ is the wavelength, $\overline{RCS}$ and $\overline{r_{RAD}}$ are reference values for radar cross-section and distance between object and observer respectively.

Even when all the above constraints are satisfied, other elements can affect the measurement acquisition process, such as:

- *Weather conditions*, particularly relevant for optical observations for which the sky has to be clear of clouds. To implement this constraint in IRIS, all measurements that do not satisfy the condition reported in Eq. (2), are discarded.

$$U_{weather}(0,1) > CCP/100 \tag{2}$$

  $U_{weather}(0,1)$ represents an uniform distribution in [0,1], whereas CCP (Cloud Coverage Percentage) indicates the percentage of nights clear of clouds.
- *Post processing errors*, mainly due to possible failures in the operations performed after the measurement process (e.g. a tracklet too close to a star mark in the CCD of optical sensor might complicate the computation of the tracklet center and produce an inaccurate measurement). To account for this phenomenon, all measurements that do not satisfy the condition in Eq. (3) are neglected.

$$U_{pp}(0,1) > DRP/100 \tag{3}$$

  where $U_{pp}(0,1)$ represents an uniform distribution in [0,1], whereas DRP (Detection Rate Percentage) represents the percentage of successful measurements.

2.2 Sensor Model

The generation of measurements occurs by combining the relative geometry with the sensors specifications. Several aspects need to be taken into account, such as:

1) *Interception probability*. The probability of detecting an object depends on the error in the expected time of arrival (derived from the positional ephemeris error σ_α) as well as on its angular velocity. The net contribution of the two generates a trigger offset that can span up to 1.5s, depending on the hardware used;

2) *Seeing phenomenon*. Random displacements and distortions in the image due to irregular and turbulent atmospheric layers. The influence of this phenomena on the observations depends on the angular velocity of the object, but typically an error of few arcseconds should be considered and added directly to the measurement error;

3) *Shutter delay calibration*. The closure of the camera is usually performed through a mechanical shutter, whose motion suffers of a certain delay (not uniform across the image). Values of 50ms and local variability of 10-50ms are typical;

4) *Timestamp acquisition*. Despite the use of dedicated hardware/lines to signal the time of acquisition, an error of few milliseconds should be considered;

5) *Astrometric calibration*. To compensate for mechanical imperfections of the mount, atmospheric refraction, as well as the daily and yearly aberration, a good astrometric calibration is generally needed and performed by pairing the stars found in the image with reference stars from catalogs. This process takes up to 1 s of exposure;

6) *Determination of tracklet apex*. To link the time domain (shutter actuation) with the spatial domain (position of the image), barycenter calculations or ellipsoid fitting algorithms can generally be adopted. In several cases a simpler approach could also be used, fitting the theoretical tracklet pattern with a straight segment. A typical accuracy of 0.3 pixels can be achieved, which translates into an error of few arcseconds;

7) *Readout time*. Reading from CCD cameras usually requires the charge to be shifted out of the photosensitive plane one pixel at a time. This allows easing the calibration process and reducing the overall noise of the instrument, but it is generally a slow process. Few seconds is the order of magnitude usually required.

Despite their importance and in order to keep the sensor models representation as simple as possible, all these aspects are summarized in IRIS in terms of random (noise) and systematic (bias) errors. More specifically, the measurement noise is described by a normal distribution with zero mean and a standard deviation equal to σ_{noise}, as indicated by the following expression:

$$m^{true} = m^{sim} + \aleph(0;\ \sigma_{noise}) \tag{4}$$

where m^{true} and m^{sim} are the real and simulated measurement, respectively.
The value of σ_{noise} is obtained as:

$$\sigma_{noise} = \sqrt{{\sigma_m}^2 + {\sigma_{seeing}}^2} \tag{5}$$

where σ_m is the typical accuracy and σ_{seeing} refers to the previous described seeing errors. In this way, all the disturbance effects due to optical geometry, media transmission and others are included. For what concerns bias errors, values equal to the resulting σ_{noise} are assumed for both optical and radar sensors.
The remaining effects, such as the intersection probability, the time stamp accuracy, the astrometric calibration and finally, the readout time, contribute to the definition of quantities like the minimum exposure time and the minimum observation window duration. In particular, a minimum exposure time of 12 seconds (10 seconds plus 2 seconds of delay) and a minimum observation window duration of 1 minute are assumed. Note also that for a given observation window, one measurement centered in the middle of the window is considered.

3. ARCHITECTURE DEFINITION

In IRIS, the procedure for the creation of observatory kernels not only allows one to work with existing sensors, but also gives the possibility to define new ideal observatories, placed at different locations on the Earth's surface or characterized by different features. Let us introduce the following distinction:

a) *Existing Architecture*, ad-hoc network composed by five existing sensors (three radar and two optical instruments);
b) *Ideal Architecture*, enlarges the ad-hoc network through the addition of new sensors, placed on the Earth surface and satisfying a set of geographical and political constraints.

3.1 Parametric Analysis

In the case of ideal architecture some analyses are needed to identify:

1) The type of observatories (optical and radar);
2) The most promising locations, keeping in mind political and physical constraints (i.e. average atmospheric conditions, illumination and sky background conditions, etc.).

Thus, a parametric analysis is carried out as follows:

i. The Earth surface is discretized using a grid of 24x12 squared elements. Consequently, the dimensions of each element are 15°x15°;
ii. Ideal observatories are placed at the center of each element, characterized by the hypothetical features in Table 1 (reasonable assumptions are made for noise figures, based on literature values);
iii. Given a space object, the number of available measurements for each site is determined through multiple runs of the IRIS tool;
iv. The same simulation is repeated for all the considered objects and for different epochs, to average object dependent and epoch dependent effects;
v. The locations with higher measurements density are identified on the Earth surface (see Fig. 2 and Fig. 3).

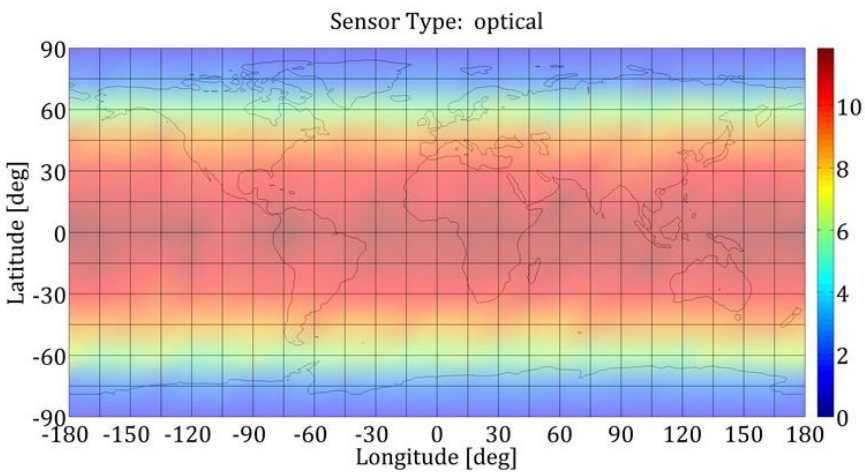

Fig. 2. Mean number of available observations for optical sensor.

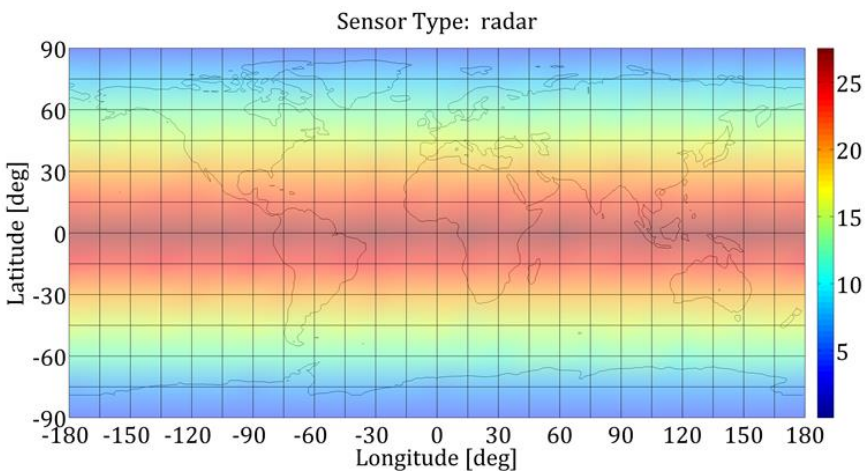

Fig. 3**.** Mean number of available observations for radar sensor.

It turns out that optical sensors provide the maximum mean number of measurements when located in the latitude band +45°/-45° (including all longitudes). Similarly, radar observatories provide the higher number of measurements (in average) when placed in latitude band +30°/-30°. These results have to be filtered in accordance with geo-political and weather constraints:

1) optical observatories should be placed at altitude higher than 1700 m and in low-densely populated areas in order to guarantee a clear sky and low light pollution;
2) for optical observations, the percentage of cloud coverage should be lower than 60%;
3) sensors should preferably be located in European territories.

Table 1. Features of hypothetic optical/radar sensors used for the ideal architecture (reported values are invented).

Features	**Optical**	**Radar (monostatic)**
Observable	Azimuth, Elevation	Range, Azimuth, Elevation, Range rate
Elevation Constraints [deg]	$\begin{bmatrix} 10 \\ 90 \end{bmatrix}$	$\begin{bmatrix} 10 \\ 90 \end{bmatrix}$
Azimuth Constraints [deg]	$\begin{bmatrix} 0 \\ 360 \end{bmatrix}$	$\begin{bmatrix} 0 \\ 360 \end{bmatrix}$
Max. Detectable Visual Magnitude	20	-
FOV [deg]	0.7	-
Time of Exposure [s]	12	-
Measurement Noise Error (σ_{noise})	$\begin{bmatrix} 0.00034\ [\mathrm{deg}] \\ 0.00034\ [\mathrm{deg}] \end{bmatrix}$	$\begin{bmatrix} 20\mathrm{e}-3\ [\mathrm{km}] \\ 0.3\ [\mathrm{deg}] \\ 0.3\ [\mathrm{deg}] \\ 0.5\mathrm{e}-3\ [\mathrm{km/s}] \end{bmatrix}$
Bias Error (σ_{bias})	$\begin{bmatrix} 0.00034\ [\mathrm{deg}] \\ 0.00034\ [\mathrm{deg}] \end{bmatrix}$	$\begin{bmatrix} 20\mathrm{e}-3\ [\mathrm{km}] \\ 0.3\ [\mathrm{deg}] \\ 0.3\ [\mathrm{deg}] \\ 0.5\mathrm{e}-3\ [\mathrm{km/s}] \end{bmatrix}$
Cloud Coverage (%)	depending on sensor location (see Table 2)	-
Weather Loss [dB]	-	-0.1
TX Power [MW]	-	1.3
Frequency [GHz]	-	1.333
TX/RX Gain [dB]	-	50
Minimum Detectable Signal [MW]	-	3.15e-19
$\overline{r_{RAD}}$ [km]	-	1000
$\overline{RCS}$ [m^2]	-	1

From these guidelines the selected locations for optical observatories are:

a) the *Andes* through Chile and Peru;
b) the *northwest America*, i.e. mountain range in Colorado, New Mexico, Utah, and Arizona;
c) the *islands in Mediterranean Sea*, such as Cyprus or Crete;

The selected sites for radar instruments are instead:

d) *Netherlands Antilles*, such as Curaçao;
e) *French Guyana*, as Kourou.

In light of the above, Fig. 4 and Table 2 report the considered locations in which the new observatories (4 for optical and 2 for radar sensors) might be placed to obtain a high number of measurements while satisfying previous guidelines. Note that these locations are merely assumptions, needed to run our computations.

Table 2. Considered sites for optical/radar additional observatories.

Sensor type	Name	Site coordinates	Altitude [m]	Mean annual cloud coverage [%]	State
Optical	Observatory O1	15° 50'S 70°01'W	3827	50	San Carlos de Puno (Perù)
Optical	Observatory O2	32° 41'N 109°55'W	2894	40	Mount Graham (Arizona)
Optical	Observatory O3	24° 37' S 70° 24' W	2635	<10	Cerro Paranal (Chile)
Optical	Observatory O4	35° 11' N 24° 47' E	1918	40	Mount Ida, Crete (Greece)
Radar	Observatory R1	5°9.31′ N 52°38.8′ W	Sea level	-	Kourou (French Guyana)
Radar	Observatory R2	12° 11'N 69°00'W	Sea level	-	Curaçao (Netherlands Antilles)

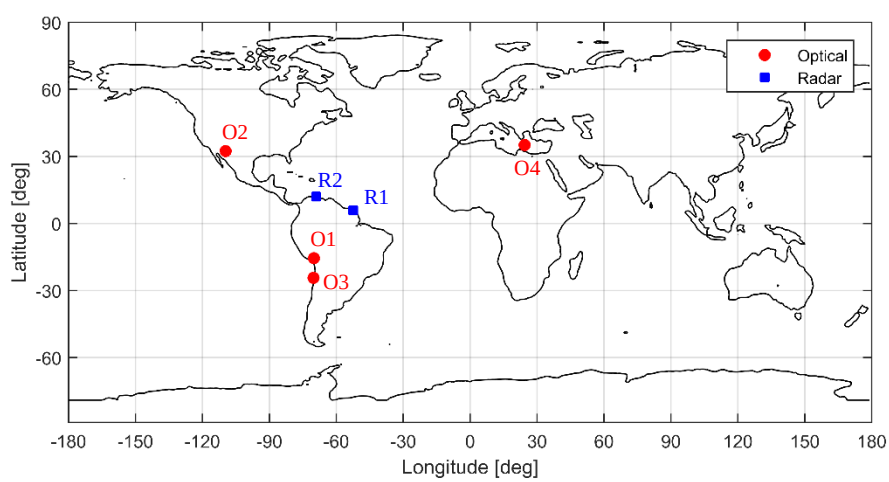

Fig. 4. Possible position of ideal observatories on the Earth's surface.

In addition to these six ideal sensors, a seventh extra observatory, referred to as N1, is added. It is located at the same coordinates of O2, but based on a new type of sensor, i.e. a Near Infrared (NIR) sensor. This type of instrument is still characterized by a low TRL and might require additional costs. However, it is interesting to investigate how its characteristics and the larger visibility windows can be exploited to improve the re-entry prediction.

3.2 Architecture Configurations

Given the set of existing sensors as well as the newly introduced ideal ones, the number of possible combinations becomes very large and cannot be easily managed. Therefore, two assumptions are introduced:

1) The five existing sensors belonging to the ad-hoc network are included in every configuration;
2) A maximum of three ideal sensors is considered.

Known this, the architecture configuration is widen following a progressive approach, including one, two and three extra sensors. At each step, the number of possible combinations is given by:

$$\frac{n!}{(n-k)!\,k!} \qquad k = 1, 2, 3 \tag{6}$$

where n is the total number of additional sensors, i.e. 7 in this case, and k is the number of additional sensors considered in the same configuration.

Table 3. Number of possible ideal architectures.

Additional sensors	N° of possible combinations
1	7
2	21
3	35

As a consequence, the total number of configurations considered in this activity is equal to 64, one corresponding to the existing architecture plus 63 for ideal ones. The identification of the best ideal architecture is performed through an optimization approach, as better described in next section.

4. OBSERVATION STRATEGY OPTIMIZATION

4.1 Optimization Approach

The main idea behind this approach is to tackle the detection strategy design problem as a multi-objective optimization problem. More specifically, the proposed optimization approach is based on the use of a multi-objective evolutionary algorithm, such as multi-objective genetic algorithm (MOGA).
The optimization approach for the strategy design consists of the following steps:

1) *Generate pseudo-observations*. For a given object and sensor architecture, the observation campaign is simulated through IRIS, starting from the reference trajectory. Through this process all the available visibility windows are computed along with the associated measurements. Jacobian matrices of the measurements, H_x, are also evaluated through the use of Differential Algebra (DA) techniques.

2) *Run MOGA*. A MOGA is run in order to minimize the number of measurements, N_{obs} and the dispersion of the re-entry epoch, $\sigma_{t_{re-entry}}$. In light of the above, the objective function is given by the following 2-dimensional vector:

$$\boldsymbol{f}(\boldsymbol{X}_{opt}) = \begin{Bmatrix} f_1(\boldsymbol{X}_{opt}) \\ f_2(\boldsymbol{X}_{opt}) \end{Bmatrix} = \begin{Bmatrix} N_{Obs} \\ \sigma_{t_{re-entry}} \end{Bmatrix}, \tag{7}$$

where X_{opt} is the optimization vector, defined as a masking vector for the set of available measurements. Since the aim is to find the optimal measurements combination, each individual in MOGA is in fact represented by a bit (0 or 1), where 1 indicates that the corresponding observation is hold, whereas 0 indicates that the corresponding observation is discarded. Therefore, $\boldsymbol{X}_{opt}$ has the form:

$$\begin{gathered} \boldsymbol{X}_{opt} = [1,0,0,1,\dots,0,0,1] \\ \boldsymbol{X}_{opt} \in \Re^{N_{Obs}} \end{gathered} \tag{8}$$

At each iteration, the following steps are performed:

i. pruning of the normal matrix $H_x^T\, W H_x$, depending on the values in the $\boldsymbol{X}_{opt}$. H_x represents the Jacobian matrix containing the partial derivatives of measurements with respect to the estimated parameters, whereas W is to so-called weighting matrix.

ii. evaluation of the computed covariance, P

$$P = \left(H_x^T W H_x \; + P_{apr}^{-1}\right)^{-1} \tag{9}$$

where P_{apr}^{-1} is the a priori information matrix.

iii. computation of $\sigma_{t_{re-entry}}$ through a linear approximation

$$\sigma_{t_{re-entry}}^2 = J_{t_{re-entry}}\, P\, J_{t_{re-entry}}^T \tag{10}$$

where $J_{t_{re-entry}}$ is the gradient of the re-entry epoch computed using finite differences.

Note that the OD process is not required in the optimization loop and thus can be avoided with large benefits on the computational speed.

4.2 Consider Covariance Analysis

The optimization approach reported in previous Section 4.1 is slightly modified to include the effects of unmodeled parameters such as bias errors [11]. The main steps are:

1) *Generate pseudo-observations*. Along with the computation of the Jacobian matrix, H_x, DA is exploited to obtain the Jacobian matrix containing the partial derivatives of measurements with respect to consider parameters, $H_c = \partial z / \partial c$. Note however that, as described also in [10], biases constitute an additive term in the general measurement equation:

$$\boldsymbol{z} = \boldsymbol{h}(\boldsymbol{x}, t) + \boldsymbol{\varepsilon} + \; \boldsymbol{c} \tag{11}$$

where $\boldsymbol{z}$ is the generic measurement, $\boldsymbol{h}(\boldsymbol{x}, t)$ is the nonlinear function of the measurement, $\boldsymbol{\varepsilon}$ is the measurement noise and finally, $\boldsymbol{c}$ represents the bias error.
Thus, the i-th element of the H_c matrix is equal to one if the station and type of the bias matches with the measurement, whereas is zero otherwise.

2) *Run MOGA*. The expression in Eq. (10) becomes:

$$\sigma_{t_{re-entry}}^2 = J_{t_{re-entry}}\, P_c\, J_{t_{re-entry}}^T \tag{12}$$

where P_c is obtained from

$$P_c = P + (P H_x^T W)(H_c C H_c^T)(P H_x^T W)^T \tag{13}$$

in which C is the covariance matrix of the considered parameters.

5. RESULTS

As already explained, the aim of this work is to devise observation strategies to improve the short-term re-entry predictions. For this reason, our analyses are mainly focused on the very last part of the trajectory, just few weeks before the re-entry. More specifically, two prediction time spans of 10 days and 20 days before the re-entry are considered. The observation time span is set to 15 days: using longer windows not only provides small improvements, but might introduce larger errors, due to the finite accuracy of the dynamical model.
The analyses are performed on a set of twenty-five objects, mainly spent upper stages, whose orbits in the last weeks before re-entry can be very different from their original orbits. In fact, due to the large changes generated by orbital perturbations, variations of 70% on the semi-major axis and 90% on the eccentricity are typical. Thus, RSO are actually moving on degraded GTO, rather than GTO.

5.1 Existing Architecture

For the sake of example, let us consider the object 24770, an Ariane 44LP H10 III stage 3. During the observation time span, the orbit further circularizes with a decrement in the semi-major axis from 9900.43 km to 8042.46 km, and with a reduction of the eccentricity from 0.34 to 0.19. Considering that the inclination is very small, about 6 deg, the tracking of this object using optical instruments becomes difficult, since most of the night is spent in the shadow of the Earth and cannot be lit by the Sun. The only visibility windows are those close to the twilight, characterized however by a limited duration. As illustrated in Fig. 5, all the measurements are obtained through the optical sensor 1 in the existing architecture, which is located at lower latitudes, and thus has a higher probability to detect objects at low altitudes and low inclinations. Other sensors, and especially radar sensors, are never able to detect the object during the whole observation time span, mainly due to elevation/power constraints.

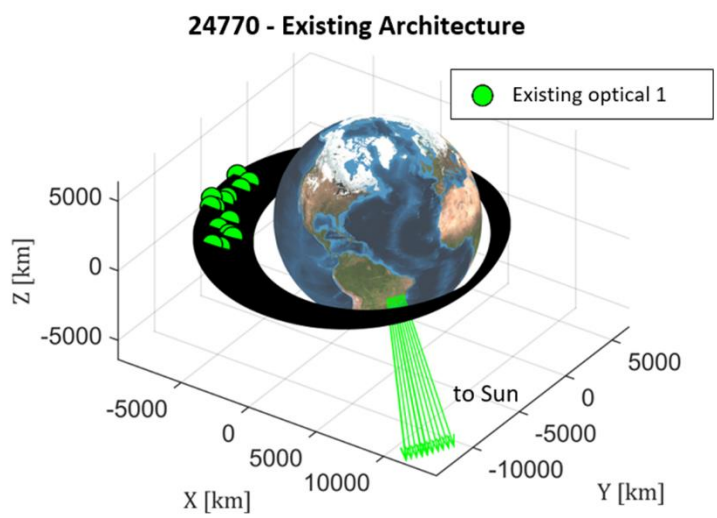

Fig. 5. 3D view of an optimal solution for object 24770.

Analogous considerations hold for the other degraded GTO objects. Fig. 6 highlights the amount of measurements obtained for all the objects through the use of the existing architecture. As can be seen, for the 10 days prediction, about 48% of the objects cannot be tracked with the sensors included in the network. Better results are found for the 20 days prediction, where the number of objects with zero measurements decreases to 36%.

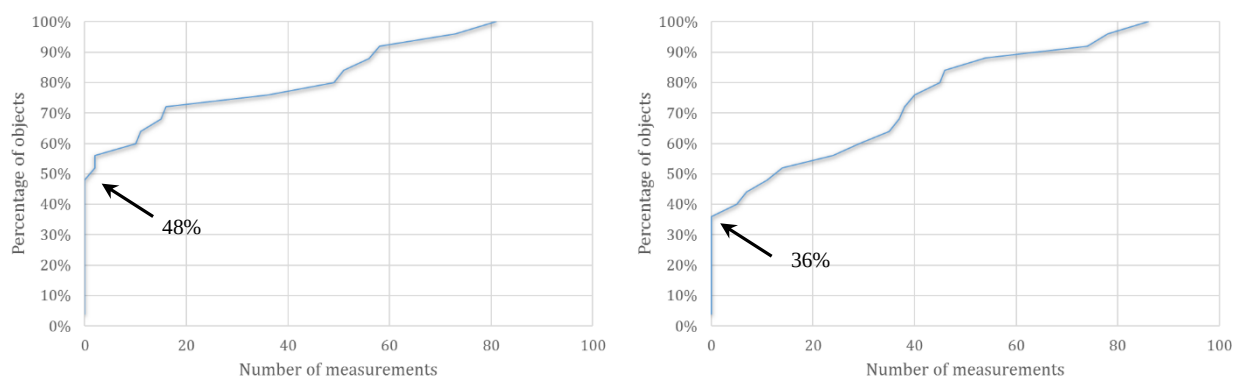

(a) (b)

Fig. 6. Cumulative density function of the number of measurements for all the objects considered. (a) 10 days prediction; (b) 20 days prediction.

Further analyses have shown that the available measurements are actually obtained from one single observatory (28% of the objects) or two different observatories (24% of the objects), whereas no object in the considered list, can be tracked by three or more observatories (see Fig. 7). Similar considerations hold also for the 20 days prediction: the only observatories used are the two optical ones, whereas the three radar instruments are never able to detect the

objects. In light of these results, it is clear that the observation of degraded GTO objects in the last few weeks before re-entry, might be difficult or even unfeasible to be performed through the sensors included in the existing architecture. This lack of observations for a large number of objects, combined with the limited amount of observatories actually used in all the other cases, also limits the strategy design process.
Two options remain: the first consists in using TLE data, accepting a typical higher re-entry dispersion, whereas the second foresees the enhancement of the ad-hoc network through the introduction of new sensors, as described in Section 5.2.

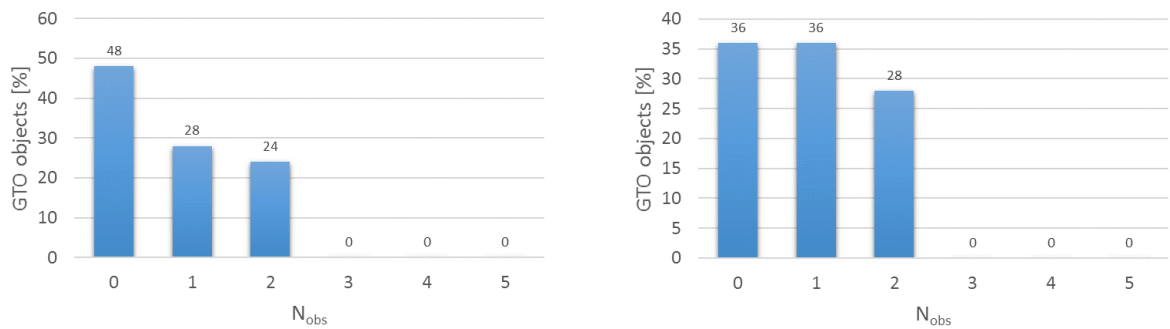

(a) (b)

Fig. 7. Number of observatories in the ad-hoc network effectively used to track degraded GTO objects. (a) 10 days prediction; (b) 20 days prediction.

5.2 Ideal Architecture

The same optimization approach has been applied to ideal configurations with one, two and three additional sensors.

One additional sensor

The major effect of adding an extra sensor to the existing architecture is represented by an increment in the number of available observation windows, and consequently in the number of measurements. This in turn, leads to a reduction of the value of $\sigma_{t_{re-entry}}$. However, the level of improvement depends on the object and the architecture configuration considered. To determine the best new sensor, a global ranking of the most promising configurations is computed, assigning highest scores to configurations with the smallest values of $\sigma_{t_{re-entry}}$.
Results are summarized in Table 4, where the best ideal architectures with one extra sensor are represented, in both prediction time spans, by those with a radar instrument in proximity of the Earth's equator.
Fig. 8 illustrates the optimal observation strategy obtained for the object 24770. Note how most of the measurements selected by the optimization process are those provided by the newly added radar sensor R1, placed at Kourou.

Table 4.Global ranking for configurations with one additional sensor.

Global position	**Architecture Configuration**	
	10 days prediction	***20 days prediction***
1ST	All existing + R2	All existing + R1
2ND	All existing + R1	All existing + R2
3RD	All existing + O1	All existing + O1

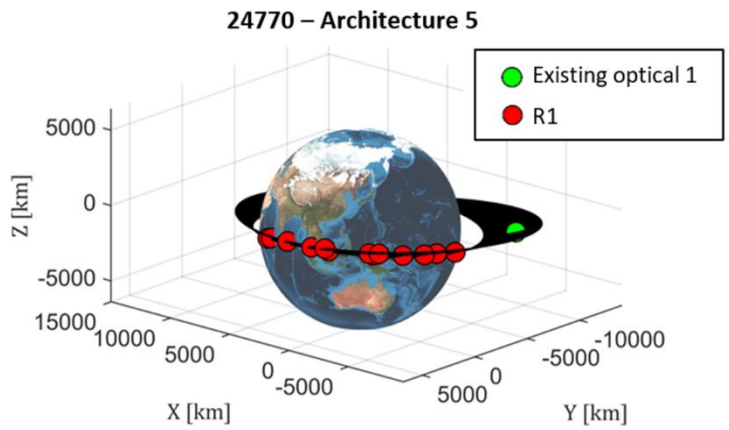

Fig. 8. 3D view of an optimal solution obtained for object 24770 with one extra radar sensor at Kourou.

Two additional sensors

The best three architectures with two additional sensors are reported in Table 5. All the reported configurations include optical and radar sensors close to the Earth's equator. In particular, for both the 10 days and 20 days prediction cases, the first position is occupied by configurations with a radar sensor at Kourou plus an additional radar at Curacao (10 days prediction) or an optical sensor in Peru (20 days prediction).

For the sake of example, results obtained for object 24770 with architecture 20 (all existing sensors + R1 + R2) are depicted in Fig. 9.

Table 5.Global ranking for configurations with two additional sensors.

Global position	**Architecture Configuration**	
	10 days prediction	***20 days prediction***
1ST	All existing + R1 + R2	All existing + R1 + O1
2ND	All existing + R1 + O1	All existing + R2 + O1
3RD	All existing + R2 + O1	All existing + R1 + R2

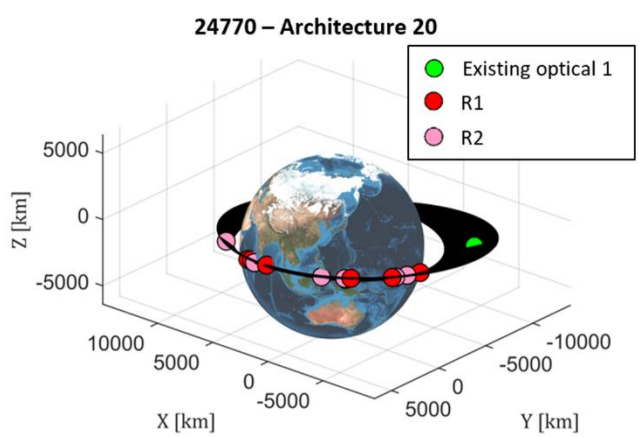

Fig. 9. 3D view of an optimal solution obtained for object 24770 with two extra sensors.

Three additional sensors

Finally, the results obtained for network configurations including three extra sensors are reported in Table 6. Even in this case, the best architecture is represented by the one in which two radars, at Kourou (R1) and Curaçao (R2), and the optical observatory in Peru (O1) are added to those already present in the ad-hoc network. Moreover, note how the use of NIR sensor provides good results, and is globally at the third position for both prediction cases.
Results for object 24770 with three new sensors are depicted in Fig. 10.

Table 6.Global ranking for configurations with three additional sensors.

Global position	**Architecture Configuration**	
	10 days prediction	***20 days prediction***
1ST	All existing + R1 + R2 + O1	All existing + R1 + R2 + O1
2ND	All existing + R1 + R2 + O3	All existing + R1 + R2 + O3
3RD	All existing + R1 + R2 + N1	All existing + R1 + O1 + N1

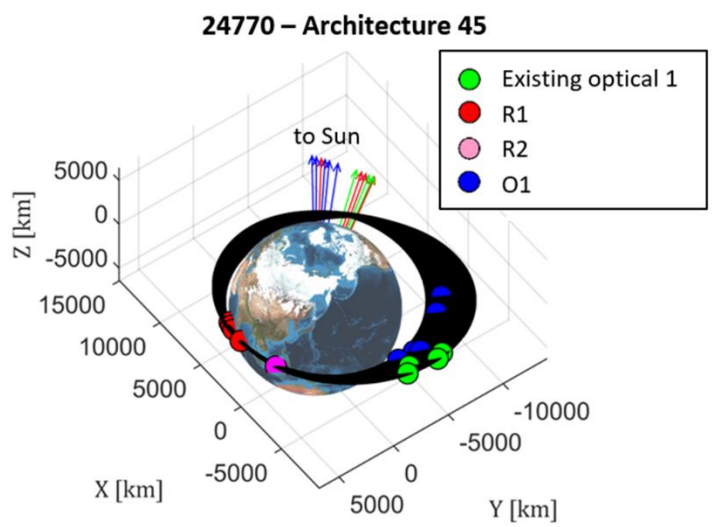

Fig. 10. 3D view of an optimal solution obtained for object 24770 with three extra sensors.

6. CONCLUSIONS

The aim of the present paper is to devise optimal observation strategies for RSO moving on degraded GTOs. Unfortunately, as seen in the provided results, the lack of measurements and the limited visibility of these objects, reduce the search space and small room is available for the optimization process. Nonetheless, the same optimization approach can be effectively used to determine the benefits on the re-entry prediction estimates, provided by the introduction of new instruments. Potential improvements can already be achieved even through the inclusion of just one radar sensor close to the equator. In fact, thanks to the significant number of available measurements, observation campaigns close to the re-entry epoch are highly enhanced and better predictions can generally be performed. Analogous considerations can be easily appreciated by looking at Fig. 11-Fig. 12, which report the relative re-entry prediction errors, defined as:

$$\lambda = \frac{3\sigma_{t_{re-entry}}}{t_{re-entry}} \text{x}100. \tag{14}$$

Note how the use of dedicated observation campaigns always ensures smaller re-entry prediction errors with respect to TLE-based methods. However, the number of trackable objects might be limited, especially when using the existing sensors in the ad-hoc network. Nonetheless, the introduction of a new radar sensor at equatorial latitudes leads to significant improvements, not just in the prediction errors, but also enlarging the number of objects that can be tracked in proximity of the re-entry. Further improvements can be obtained through the use of two or more extra sensors.

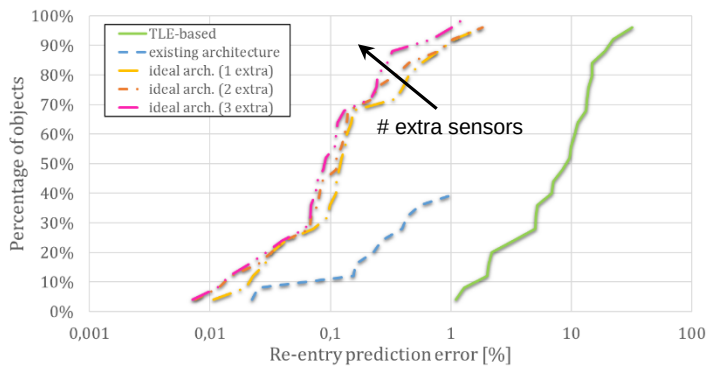

Fig. 11. Re-entry prediction error for the 10 days prediction.

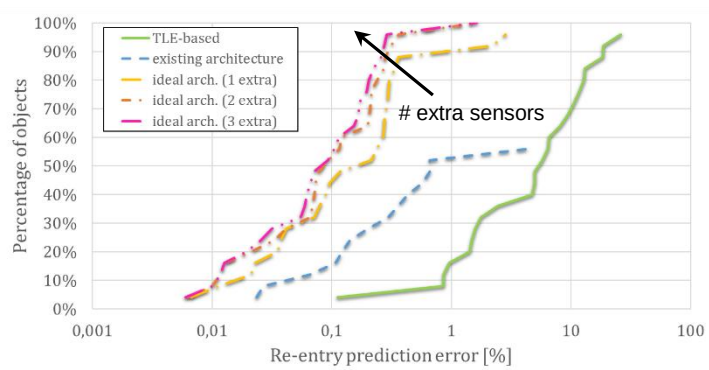

Fig. 12. Re-entry prediction error for the 20 days prediction.

Another interesting conclusion concerns architectures with NIR sensors, which turned out to be very promising, although additional costs might be required due to the early stage of this technology. Anyway, they represent very interesting solutions and for this reason might deserve dedicated analyses and further developments.
Lastly, it is worth remembering that locations and characteristics proposed for new extra sensors are fully based on assumptions for the purpose of this research paper and do not reflect actual plans.

7. ACKNOWLEDGMENTS

The presented study was performed under ESA contract ITT AO/1-8155/15/D/SR. Authors are grateful to Jan Siminski for his precious advices.

8. REFERENCES

1. IADC-02-01 *IADC Space Debris Mitigation Guidelines*, September 2007.
2. NASA Technical Standard, *Process for Limiting Orbital Debris (NASA-STD-8719.14)*, 6 September 2007.

3. E. Bowell, J. Virtanen, K. Muinonen, and A. Boattini. Asteroid Orbit Computation. In *Asteroid III*, The University of Arizona Press. 2002.
4. D.A. Vallado, B.B. Virgili, T. Flohrer, Improved SSA Through Orbit Determination of Two-Line Element Sets. *6th European Conference on Space Debris*. Darmstadt, Germany, 22-25 April, 2013.
5. A. Saunders, G. G. Swinerd, and H. G. Lewis, Deriving Accurate Satellite Ballistic Coefficients from Two-Line Element Data. *Journal of Spacecraft and Rockets*. Vol 49, No 1, Jan-Feb, 2012.
6. B. Kraus, D. DeSieno, D. Surka, G. Haith, and C. Bowman, Detecting Abnormal Space Catalog Updates. *Infotech@Aerospace Conference*, 19-21 June, 2012, Garden Grove, California.
7. J.D. Pérez, L. A. Garcia, A. Águeda Maté, and I. Llamas de la Sierra, OPERA: A tool for lifetime prediction based on orbit determination from TLE data. *24th International Symposium on Space Flight Dynamics*. Laurel, Maryland, USA, 5-9 May, 2014.
8. R.P. Patera, Space Event Detection Method. *Journal of Spacecraft and Rockets*. 45(3), pp. 554–559, 2008.
9. M. Mutyalarao, R. K. Sharma, On Prediction of Re-Entry Time of an Upper Stage from GTO. *Advances in Space Research*, Volume 47, Issue 11, p. 1877-1884.
10. Montenbruck O., Gill E., *Satellites Orbits. Models, Methods and Applications*. Springer, 2005.
11. Schutz B., Tapley B. and Born G. H., *Statistical orbit determination*. Academic Press, 2004.